7-2024

Testing of an Organic Metal Halide Perovskite for Fast Neutron Detection

Wyatt Panaccione
The Ohio State University

Zhifang Shi
University of North Carolina at Chapel Hill

Praneeth Kandlakunta
The Ohio State University

Taylor M. Nichols
Air Force Institute of Technology

Susan White
The Ohio State University

See next page for additional authors

Recommended Citation

Panaccione, W., Shi, Z., Kandlakunta, P., Nichols, T., White, S., Huang, J., & Cao, L. R. (2024). Testing of an organic metal halide perovskite for fast neutron detection. Nuclear Instruments and Methods in Physics Research Section A: Accelerators, Spectrometers, Detectors and Associated Equipment, 1064, 169340. https://doi.org/10.1016/j.nima.2024.169340

Nuclear Instruments and Methods in Physics Research A 1064 (2024) 169340

Contents lists available at ScienceDirect

Nuclear Inst. and Methods in Physics Research, A

journal homepage: www.elsevier.com/locate/nima

Testing of an organic metal halide perovskite for fast neutron detection

Wyatt Panaccione [a], Zhifang Shi [b], Praneeth Kandlakunta [a], Taylor Nichols [c], Susan White [d], Jinsong Huang [b], Lei R. Cao [a,c,*]

[a] Nuclear Engineering Program, Department of Mechanical and Aerospace Engineering, The Ohio State University, Columbus, OH, 43210, USA
[b] Department of Applied Physical Sciences, University of North Carolina at Chapel Hill, Chapel Hill, NC, USA
[c] Department of Engineering Physics, Air Force Institute of Technology, 2950 Hobson Way, Wright-Patterson Air Force Base, OH, 45433, USA
[d] Nuclear Reactor Laboratory, College of Engineering, The Ohio State University, 1298 Kinnear Rd, Columbus, OH, 43212, USA

ARTICLE INFO

Keywords:
Perovskite
Fast neutron detection
Neutron beam
Gamma-rays
Gamma discrimination

ABSTRACT

In this work, we synthesized and characterized the Methylhydrazinium Lead Trichloride $MHyPbCl_3$(CH3NH2NH2PbCl3) perovskite as a fast neutron detector. The high hydrogen density of $MHyPbCl_3$ enables efficient energy conversion from a fast neutron into a recoiled proton through the $^1H(n,n)^1H$ elastic scattering interaction, thereby, allowing for direct charge detection. Through IV characterization and X-Ray excitation, the crystal demonstrated a high resistivity at 4.43*E*11 $\Omega\,cm$ and a good mobility-lifetime product ($\mu\tau$) of 9.1E-3 $\frac{cm^2}{V}$, respectively, under C_{60}/BCP/Cu and Au contact configuration to form an ohmic-ohmic detector. The crystal showed a good sensitivity to X-rays using an x-ray tube. The feasibility of the direct neutron conversion detector is demonstrated using the fast neutron beam at a Research Reactor. Waveforms from a charge-sensitive pre-amplifier showed distinct radiation-induced pulses from the $MHyPbCl_3$ detector in response to the reactor neutron beam. Using a thermal neutron filter and gamma shielding in the beam, we showed that the pulses produced were more likely from neutron interactions, despite the Pb containing $MHyPbCl_3$ is also sensitive to gamma-rays. With those fast neutron pulses, a post-pulse processing code was used to conduct pulse height analysis (PHA) and reconstruct an energy spectrum.

1. Introduction

Fast neutron detection plays a crucial role in nuclear non-proliferation, neutron imaging, radiation therapy, materials testing, and well logging for industrial applications [1–10]. The intrinsic challenge of detecting fast neutrons stems from their high penetration capabilities, attributed to their small cross-section [11]. To counter this challenge, the prevalent detection methodology exploits the elastic scattering interaction between neutrons and hydrogen present in hydrogenous materials. Traditionally, plastic scintillators, stilbene, and innovative Organic Glass Scintillators (OGS) [12] have dominated the realm of fast neutron detectors [13,14]. The emerging materials such as CLYC (Cs_2LiYCl_6: Ce) and CLLBC ($Cs_2LiLa(Br,Cl)_6$: Ce) have also demonstrated potentials as promising alternatives [15,16]. Thermal neutron detectors, in contrast, leverage conversion materials such as Helium-3, Boron-10, Lithium-6, U-235, and Gd-157, known for their high absorption cross-section to thermal neutrons [17–20]. The utilization of fission fragments from neutron capture events facilitates the detection of these thermal neutrons. When detecting fast neutrons, the primary interaction has to be much less efficient elastic scattering process. Hence, detection efficiency often hinges on the conversion of the neutron's kinetic energy into recoiled charged particles via light elements (e.g., hydrogen or carbon), producing a detectable signal [21] (see Table 1).

A recent development in fast neutron detection is the use of plastic scintillator known as SANDD (Segmented Anti-Neutrino Directional Detector) — a tool designed for near-field reactor monitoring with sensitivity to antineutrino direction [22,23]. Similarly, Buffler et al. showcased a neutron spectrometer employing EJ-276 plastic scintillators paired with an HDPE moderator [24]. A defining feature of these scintillators is their pulse shape discrimination (PSD) capabilities, enabling a distinction between gamma rays and neutron interactions [25]. This distinction arises because of the difference in light pulses' decay times resulting from the different interaction mechanisms of

* Corresponding author. Nuclear Engineering Program, Department of Mechanical and Aerospace Engineering, The Ohio State University, Columbus, OH, 43210, USA.
E-mail address: cao.152@osu.edu (L.R. Cao).

https://doi.org/10.1016/j.nima.2024.169340
Received 10 September 2023; Accepted 7 April 2024
Available online 12 April 2024

Table 1
A table comparing the chemical formula, density, and hydrogen density of $MHyPbCl_3$, Rubrene, 4MHB, and Stilbene.

Material	Chemical Formula	Density (g/cm^3)	Hydrogen Density (cm^{-3})
$MHyPbCl_3$	$CH_3NH_2NH_2PbCl_3$	3.242	3.79 E22
Stilbene [32]	$C_{14}H_{12}$	1.15	4.61 E22
Rubrene [30]	$C_{42}H_{28}$	1.26	3.99E22
4MHB	$C_6H_5O-COOCH_3$	1.46	4.62E22

neutrons and gamma rays. Plastic scintillators, such as EJ-270, EJ-276, and EJ-301, are illustrative of this PSD capability, effectively demonstrating their proficiency in differentiating signals [26–28].

Although scintillators have traditionally been the go-to option for fast neutron detection, the promise of semiconductor-based direct charge collection cannot be dismissed, particularly when compactness and high pixelation density are the essential considerations [29]. Nonetheless, these systems face the challenge of effectively intercepting fast neutrons (requiring large volume) while maintaining favorable charge transport properties (favoring small volume). Studies have explored the prospects of organic semiconducting materials for this purpose. For instance, Carman et al. elaborated on the utility of rubrene crystals as detectors for both alpha particles and neutrons, with proven effectiveness in capturing the neutron spectrum emitted from a Californium-252 source [30]. Similarly, Zhao et al. unveiled the use of organic semiconducting single crystal detectors to detect both alpha and fast neutron spectrums from an AmBe isotopic neutron source [31]. Our work introduces Methylhydrazinium Lead Trichloride ($MHyPbCl_3$) as a novel semiconductor for fast neutron detection. With a hydrogen density comparable to that of Stilbene and Rubrene and possessing robust electrical transport properties, this material, $MHyPbCl_3$, shows promises for fast neutron detection, although Pb still poses challenges for gamma-ray discrimination.

2. Methods

2.1. Methylhydrazinium chloride (MHyCl) synthesis

To obtain MHyCl 2.63 mL (50 mmol) methylhydrazine (MHy) was diluted with 5 mL anhydrous isopropanol (IPA) and then 100 mL 0.5 M HCl was added to the IPA solution without stirring. The MHyCl precipitated as white plate crystals after this mixed solution was stored overnight in an inert atmosphere at room temperature. The crystals were filtered and washed with cold IPA solvent, then dried under vacuum at room temperature, yielding 3.10 g (~38%).

2.2. $MHyPbCl_3$ single crystal growth

$MHyPbCl_3$ single crystals were grown using the anti-solvent assisted crystallization method. Briefly, 2 mmol MHyCl and 2 mmol $PbCl_2$ were dissolved in 5 mL DMF and 1 mL DMSO. After stirring for 3 h, the solution was filtered through a 0.22-μm filter to remove the undissolved particles into a 20 mL vial. This vial-filtered solution was then transferred to a 100 mL bottle containing 15 mL of toluene (TL) as an anti-solvent and sealed in the glovebox. After 1 week, several clear hexagonal crystals formed. The crystals were harvested and then dried under vacuum. The crystals were polished with polishing paper to remove the polycrystalline layer on the surface prior to electrode deposition.

2.3. Fast neutron beam facility

The Fast Beam Facility (FBF) at the Ohio State University Research Reactor (OSURR) is equipped with a fast neutron collimator that incorporates a 4-inch thick (10.16 cm) single crystal Bismuth gamma filter and an 8-inch thick (20.32 cm) lead (Pb) gamma shutter which is embedded inside the reactor's concrete wall. Additional thermal neutron filtering, often using a 2-mm thick Cd foil, can be added externally at the beam exit for thermal neutron removal. The gamma shutter consists of an 8-inch (20.32 cm) diameter drum filled with 1/16" (0.159 cm) lead shot. When open, the neutron beam travels through an air gap, and when closed, it's attenuated by the lead shot. In total, the lead shot offers about 8 inches of gamma shielding.

Upon closure of the gamma shutter, the gamma-ray content within the beam decreases by a factor of 311, concurrently attenuating fast neutrons by a factor of 58. This configuration yields a neutron beam featuring a fast neutron flux of 2.6E5 $cm^{-2}s^{-1}$ and a cumulative gamma dose of 50 mR/h, as depicted in row 4 in Fig. 1B. Incorporating an external Cd filter will have a minimal effect on the epi-thermal neutron counts. As a result, the epi-thermal neutron count is estimated at 2.6e5 $cm^{-2}s^{-1}$ (row 5 in Fig. 1B). Meanwhile, the estimation of thermal neutron content is determined by the thermal neutron reduction factor of 110 (calculated as the ratio of 7.9E6/7.1E4, as described in rows 2 and 3 in Fig. 1B). Consequently, a reduction of a factor of 110 from the thermal neutron content (2.5E4 $cm^{-2}s^{-1}$ in row 4 in Fig. 1B) yields the estimated thermal neutron content at 220 $cm^{-2}s^{-1}$ when both the gamma shutter closed and the Cd filter applied. Although the uncertainty in the estimated thermal neutron flux is conservatively set at <20%, this flux level is valuable for evaluating neutron detectors, as it is well collimated and sufficiently low to mitigate pulse pileup effects.

The neutron beam energy spectrum, without the Pb gamma shielding, can be observed in Fig. 1A, which was determined using the SAND-II and STAYSL spectrum unfolding techniques with Cu, Au, and Ni metal wire neutron activation. Although the fast neutron flux wasn't evaluated with the Cd filter, cadmium's expected impact is minor. The Cd filter's ability to reduce thermal neutron flux was verified using Au foil reaction rate calculations, based on the ASTM E262-17 standard, yielding a Cadmium Ratio of 1.1 and a subsequent thermal flux reduction factor of 110.

2.4. Data acquisition

Fig. 3C and D show the experimental setup of the FBF and the respective experiment setup. For assessing the device's fast neutron detection capability, samples were placed in the FBF and connected with a CAEN 1422 charge-sensitive preamplifier. The ensuing pulses generated by this preamplifier were fed into a Tektronix MSO54 oscilloscope and subsequently saved onto a thumb drive. Given that these pulses did not exceed 15 mV, they required post-processing for noise filtration and subsequent data analysis. Experiments were conducted both with and without lead gamma shielding in place. Notably, due to electronic noise, the detector's voltage bias was capped approximately at 120 V.

Data from the experiment was processed using a Python-based pulse height analysis code. This software facilitated the import of.mat files, which underwent refinement via a Locally Weighted Scatterplot Smoothing (LOWESS) algorithm—integral for enhancing the low amplitude signal clarity. Following the application of the LOWESS filter, a baseline correction was performed on the dataset, and pulse heights were determined based on the peak data points. These pulse heights were then presented in a histogram format for further analysis.

3. Results and discussion

3.1. $MHyPbCl_3$ direct conversion theory

Fast neutrons, due to their absence of electric charge and minimal interaction with matter, are challenging to detect. High hydrogen density materials often act as conversion medium, facilitating neutrons' elastic scattering. While perovskites have seen being used in neutron detection, this has primarily been confined to indirect methods. Specifically, 2D perovskites with extended linear ligands have been employed as scintillators to transform neutrons into visible lights [33],

A

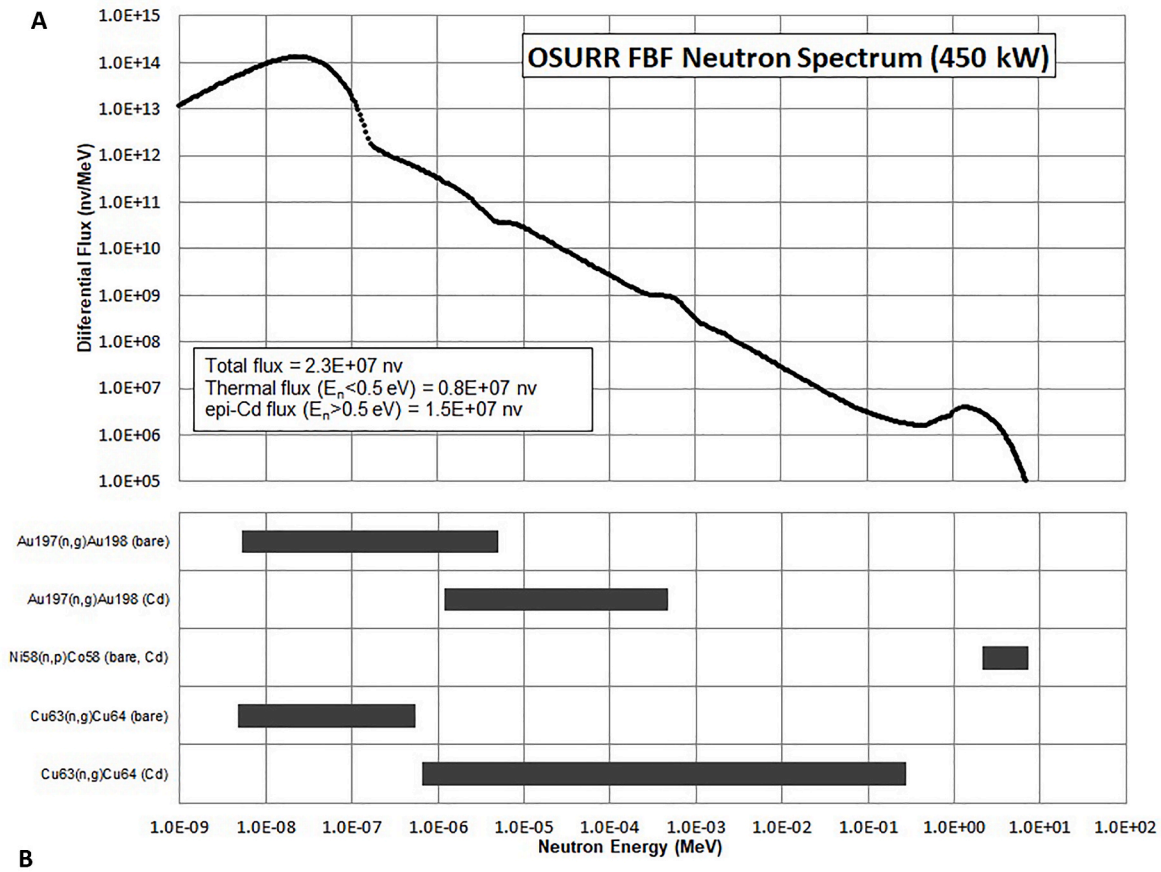

B

Fast Neutron Beam Configurations	Epi-thermal flux, ($cm^{-2}s^{-1}$)	Thermal flux, ($cm^{-2}s^{-1}$)	Gamma dose rate, $\frac{mR}{hr}$
Gamma Shielding: No Thermal Neutron Filter (Cd): No	Integrated (En>0.5 eV): 1.5E+7	Integrated (En<0.5 eV): 8.3E+6 2200 m/s: 7.9E+6	15,750
Gamma Shielding: No Thermal Neutron Filter (Cd): Yes	~ 1.5E+7	2200 m/s: 7.1E+4	15,750
Gamma Shielding: Yes Thermal Neutron Filter (Cd): No	Integrated (En>0.5 eV): 2.6E+5	Integrated (En<0.5 eV): 2.6E+4 2200 m/s: 2.5E+4	50
Gamma Shielding: Yes Thermal Neutron Filter (Cd): Yes	~2.6E+5	2200 m/s: ~ 2.2E+2	50

Fig. 1. (A) Neutron lethargy spectrum of the fast neutron beam measured using neutron activation of metal and spectrum unfolding. (B) A matrix with the epi-thermal neutron, thermal neutron, and gamma ray components of the beam under the different beam shielding configurations.

which are detected by a subsequent photodetector. In contrast, 3D perovskites like $MAPbBr_3$ and $FAPbBr_3$, despite their superior carrier transport capabilities, aren't suitable for fast neutron detection due to their reduced hydrogen density.

In Fig. 2A, we assess the hydrogen density across various dimensional and halide perovskites. Notably, 2D perovskites exhibit a higher hydrogen density than their 3D counterparts, attributed to their expansive organic spacers. In particular, Methylhydrazinium lead trichloride ($MHyPbCl_3$) boasts a hydrogen density nearly mirroring that of the frequently utilized phenethylanium lead iodide (PEA_2PbI_4). Yet, it retains a 3D inorganic framework, as demonstrated in Fig. 2B [34]. Using the anti-solvent vapor-assistant crystallization technique, we synthesized transparent MHyPbCl3 single crystals, measuring up to $3 \times 3 \times 0.7$ mm^3. Fig. 2C exhibits the powder X-ray diffraction patterns of $MHyPbCl_3$, underscoring its anticipated monoclinic 3D structure. We then constructed a device with the configuration: Cu/BCP/C60/$MHyPbCl_3$/Au.

We selected Methylhydrazinium ($CH_3NH_2NH_2$) as the organic cation, given its unmatched hydrogen density in a 3D ABX_3 perovskite structure. Hydrogen's relatively high fast neutron scattering cross-section enables the creation of ionized hydrogen atoms, essentially protons, which generate electron-hole pairs. When a bias is applied, these pairs can be gathered and quantified.

3.2. Device characterization

To ensure the device can produce a discernible pulse and maintain a low leakage current, it is imperative to employ a highly resistive material with minimal charge trappings. Post-device fabrication, the device's resistivity was gauged through current-voltage (I–V) characterization, and it was determined to be 4.43E11 Ω cm. Taking into account our prior experience with perovskite-based detectors, an operational bias range of 35 V was deduced, aiming to keep the leakage current below 10 nA. Exceeding this current can introduce increased noise and destabilize the device. For this study, however, we operated within a range of 80 V–120 V, optimizing charge collection while ensuring stable performance. Fig. 2D displays the on-off curve under X-ray radiation, with the device's X-Ray sensitivity registering at 61.74 μC Gyair cm^{-2}, as illustrated in Fig. 2E, which presents the X-Ray induced photocurrent across various X-Ray fluences. The mobility-lifetime product (μτ) is deduced by aligning the steady-state X-ray current-bias curves with the refined Hecht equation, as highlighted in Fig. 2F. Notably, the μτ of $MHyPbCl_3$ stands at 9.1E-5 cm^2/V, marking a significant improvement, nearly two orders of magnitude greater than that of 2D perovskites such as PEA_2PbI_4 [31].

3.3. Simulation

Monte Carlo simulations, using GEANT4 [35,36], were employed to validate the viability of using $MHyPbCl_3$ for fast neutron detection and to anticipate the detector's performance in the experimental setup. Within Geant4, a model of the perovskite slab (representing the detector) was created, mirroring the dimensions of the perovskite layer in our actual device. We used a disk source of neutrons mirroring the OSURR FBF spectrum to emulate the scenario where the detector is exposed to a fast neutron beam. The energy deposition in the perovskite resulting from direct neutron impacts was determined. For comparison, simulations were also run replacing the detector material with Stilbene. Fig. 4A contrasts the energy deposition spectra of MHy and Stilbene detectors. Notably, even with comparable hydrogen densities, the MHy detector showcased slightly elevated energy deposition. This heightened deposition in MHy is potentially due to the presence of nitrogen and chlorine, both of which increase neutron scattering interactions. Though the elastic scattering cross sections for nitrogen, chlorine, and hydrogen are relatively similar, the concentration of chlorine and nitrogen is markedly less than hydrogen. Fig. 4C emphasizes the effects of using a Cd filter. By absorbing a majority of thermal neutrons, the Cd filter showcased that thermal neutron interactions amplify the energy deposition in

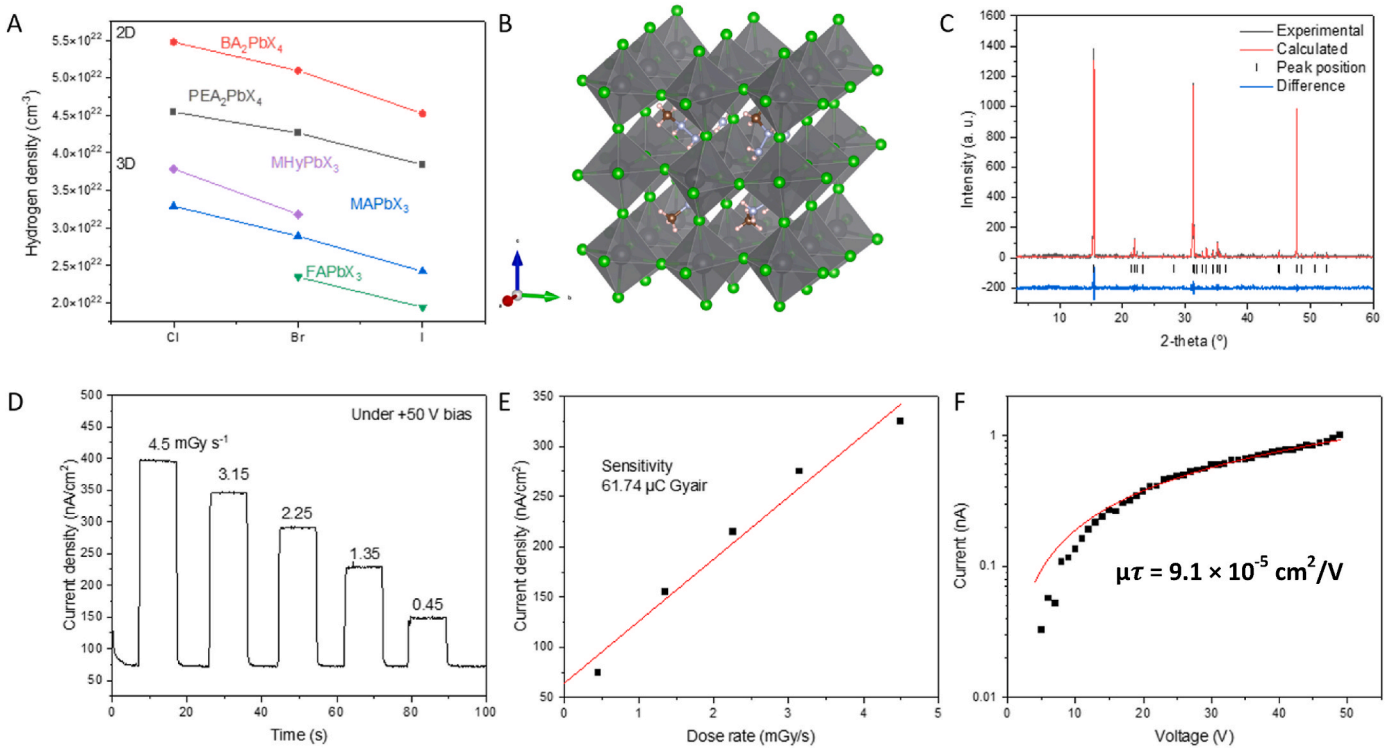

Fig. 2. Design and characterization of MHyPbCl3. (A) hydrogen density of 2D and 3D perovskites. (B) structure schematic of MHyPbCl3. (C) powder X-ray diffraction patterns. (D) on-off curves of a MHyPbCl3 device under X-ray radiation. (E) Response of MHyPbCl3 device under X-ray radiation. (E) μτ product derived by fitting the steady-state X-ray current-bias curves with the modified Hecht equation.

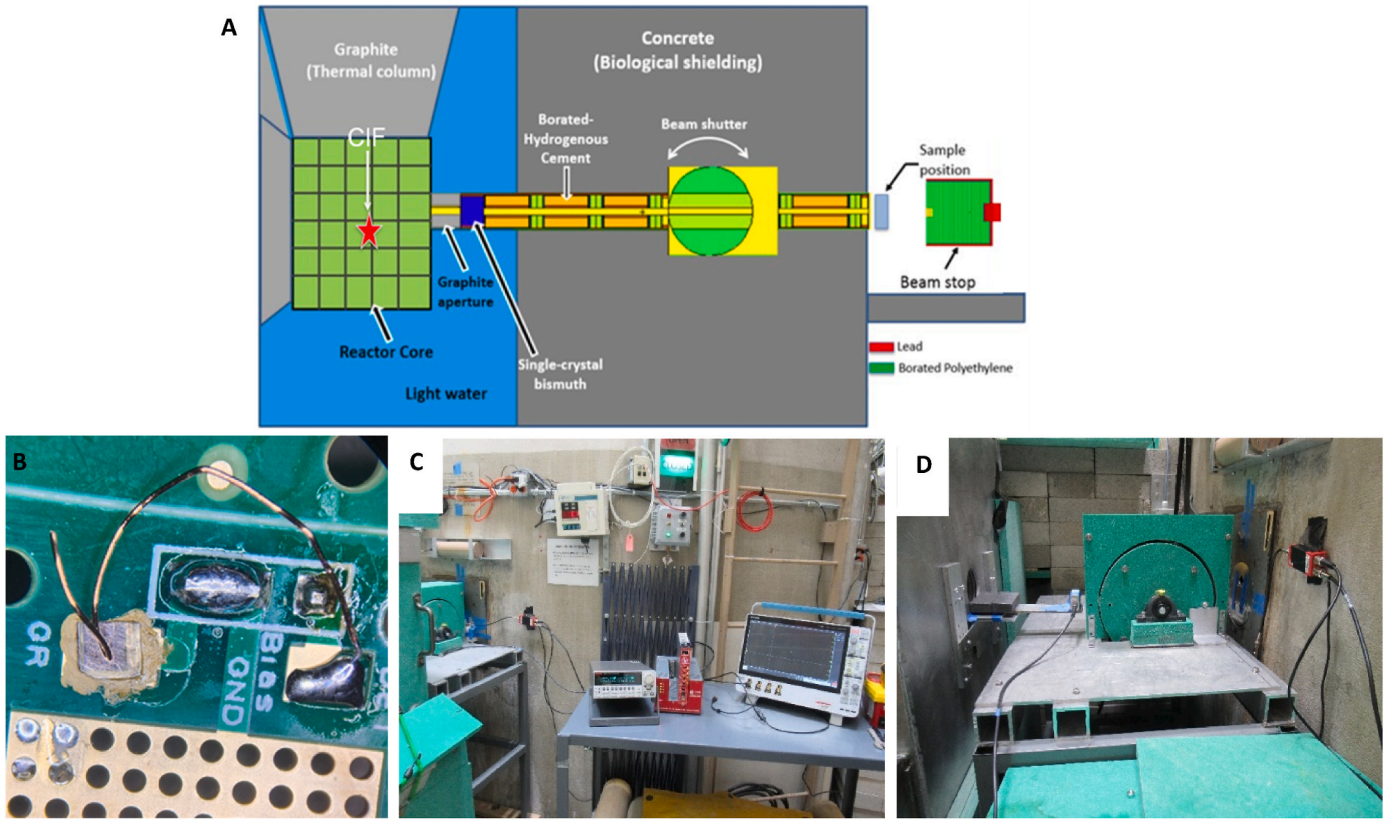

Fig. 3. (A) Schematic of the FBF at OSU Research Reactor. (B) An image of the device mounted on a PCB board for testing. (C) Image of the FBF and data acquisition setup used to measure the response. (D) An image of the FBF chopper that was used to aid in the mounting of the detector.

the MHy detector slightly, mainly in the lower energy regime.

An additional Monte Carlo simulation was conducted using MCNP6 to determine the viability of the $MHyPbCl_3$ device to characterize neutron energy sources, specifically those of nuclear weapon detonations. The results are shown in Fig. 4B. Using the F6 tally, the energy deposition from incident neutrons and secondary gamma-rays was simulated for each layer of the photovoltaic device. Each layer of the device is 5 cm by 5 cm with varying thicknesses and materials according to the physical parameters of the experimental device: 80 nm thick copper (69% Cu-63 and 31% Cu-65), 6 nm thick bathocuproine ($C_{26}H_{20}N_2$), 30 nm thick carbon (100% C-12), 0.7 mm thick Methylhydrazinium Lead Chloride ($CH_3NH_2NH_2\ PbCl_3$), and 80 nm thick gold (100% Au-197). This device model was executed with two different radiation point sources for comparison: the Fat Man neutron spectrum source and a 1 MeV isotropic neutron source. The 1E6 neutron source was placed 1 km away from the multi-layered device and the environment was modelled as nitrogen-rich air. The $MHyPbCl_3$ layer of the device had the highest energy deposition from incident neutrons for both sources at 1.15E-3 MeV per source particle for the Fat Man neutron spectrum source model and 1.26E-3 MeV per source particle for the 1 MeV isotropic neutron source model. Additionally, this layer had the highest energy deposition from secondary gamma-rays for the Fat Man neutron spectrum source model at 3.08E-03 MeV per source particle. The remaining four layers of the device had lower energy depositions by at least two orders of magnitude difference or more. The results from this study determined that the $MHyPbCl_3$ device is a viable candidate for neutron detection.

3.4. Neutron and gamma discrimination

For any neutron detection system, discriminating gamma rays is paramount. To establish that our detector's response was indeed from fast neutrons, we estimated the gamma discrimination on simulations-based counting statistics and the experimental beam characterization. Fig. 5 depicts the components in the fast neutron beamline, encompassing fast neutrons, thermal neutrons, and gamma rays. Two main filters were employed: a gamma shutter within the collimator, aimed at blocking gamma emissions from the reactor core, and a Cd filter to eliminate majority of thermal neutrons. Without the 8-inch lead gamma shielding, the fast energy regime's neutron flux is 1.5E7 $cm^{-2}s^{-1}$. With the shielding engaged, this rate plummets 58-fold to 2.6E5 $cm^{-2}s^{-1}$. As discussed in section 2.3, Fig. 1B details the beam's thermal, fast (inclusive of epithermal), and gamma components under various configurations.

To discern the neutron response in the presence and absence of gamma shielding, we analyzed the count rates. Given the understood reduction in neutron and gamma components, similar count rate reductions were anticipated, assuming the detector linearly responds to both neutrons and gamma rays. If count rates diminish akin to gamma shielding's reduction factor, it suggests the response is predominantly due to the beam's gamma component and vice versa.

Our initial $MHyPbCl_3$ detector posed a challenge due to the crystal's limited size—a mere 330 μm thickness. While this reduces detection efficiency for fast neutrons, it inadvertently offers lower gamma ray detection efficiency too. We evaluated the gamma-ray attenuation probability to discern the expected gamma reaction rate. For gamma rays at 100 keV and 1 MeV, interaction probabilities stood at 28% and 0.07%, respectively. Meanwhile, elastic scattering of 1.6 MeV neutron interactions exhibited a 0.437% probability. This underscores the device's stronger inclination towards fast neutron interactions, with only low-energy gamma rays posing a genuine challenge. To counteract this, gamma shielding was incorporated, focusing on attenuating lower-energy gamma rays. While we cannot wholly eliminate high-energy gamma rays or prompt gammas resulting from neutron captures, for

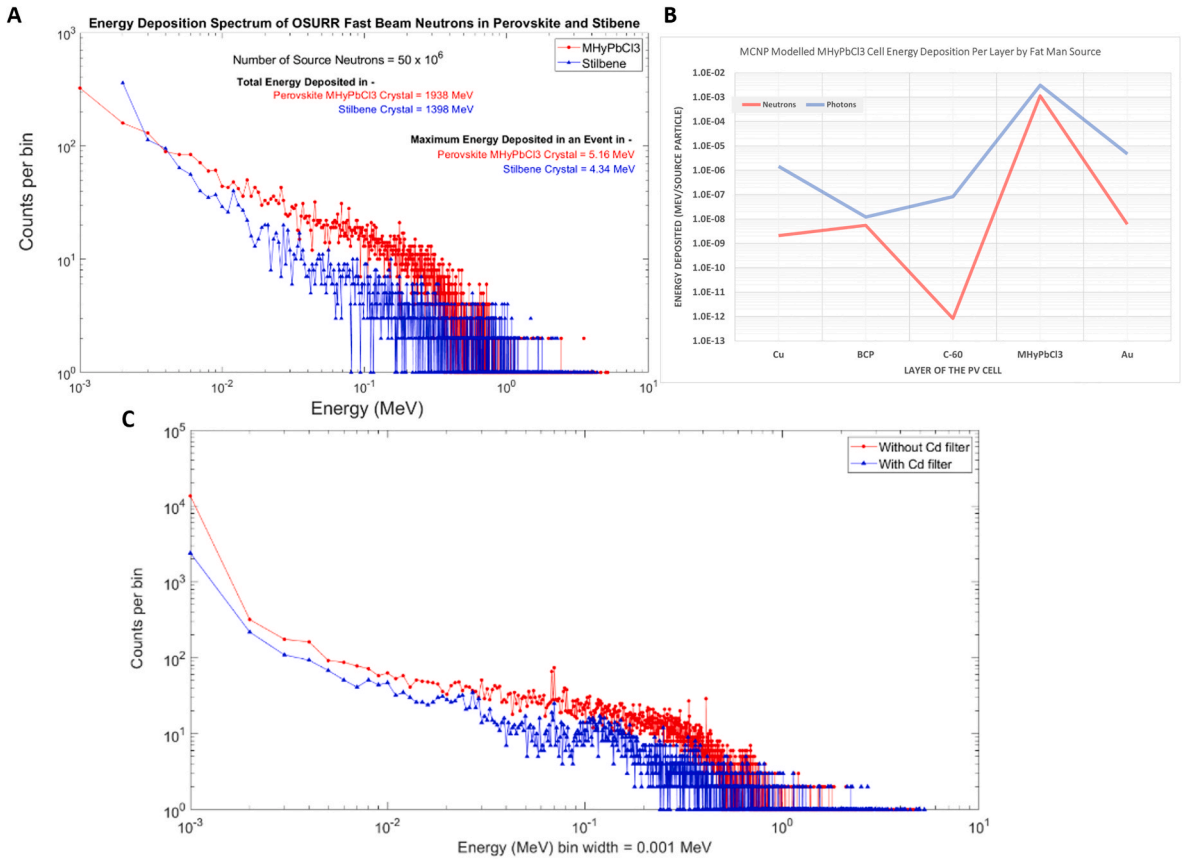

Fig. 4. GEANT4 simulations results of (A) a comparision between the energy deposited into the $MHyPbCl_3$ and stilbene crystals of same size. (B) Results from MCNP6 for energy deposited in the different layers from the Fat Man neuton spectrum and monoenrgetic 1 MeV. (C) simulated results of energy deposition in $MHyPbCl_3$ with and without the thermal neutron filtered by Cd.

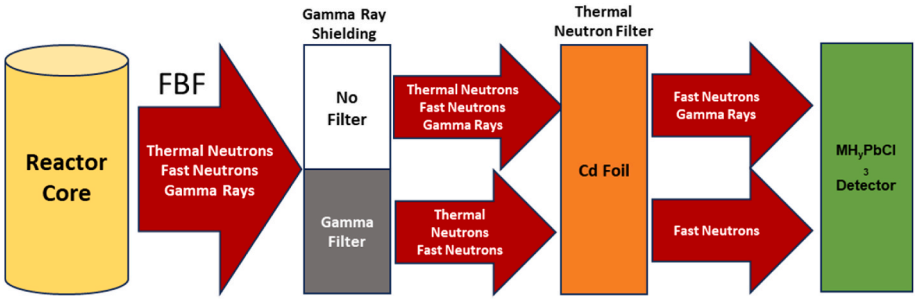

Fig. 5. A diagram of the capabilities of the FBF and how the thermal neutron and gamma shielding create a beam with majority being fast neutrons.

this study's context, the data suggested that the detector is more aligned to detecting fast neutrons over gamma rays. The different neutron interaction probability relative to gamma rays, combined with the varying neutron and gamma ray reduction ratios with/without gamma shielding, suggested that aligning the count rate with the reduction ratio of the fast neutron component is satisfactory.

3.4.1. Results with testing MHyPbCl3 in neutron beam

Radiation response testing of $MHyPbCl_3$ in the fast neutron beam was executed both with and without lead gamma shielding. Due to elevated noise levels at higher voltages, we capped the detector's bias at about 120 V. Even with the limitations of charge collection efficiency and restricted bias in this pioneer direct-conversion fast neutron detector, we still observed voltage pulses. Oscilloscope readings, post-moving linear regression filtering, are shown in Fig. 6A and B. When contrasting outcomes with and without gamma shielding, it becomes apparent that any major pulses are a result of gamma rays in the beam. The diminished pulse count in Fig. 6B can be attributed to the reduced fast neutron flux when the gamma shielding is active and to the detector's inherent sensitivity to gamma rays in the beamline.

The device exhibits a rather protracted rise time, lying between 20 and 50 μs. This offers a semblance of evidence for the potential use of semiconductor pulse shape discrimination (PSD) in discerning between neutron and gamma events [37]. Still, equating pulse rise time directly with singular gamma or neutron events proved unfeasible. We tried to understand the detector's response by examining the gamma component in the beam, gauging the gamma dose rate. The gamma shutter's deployment curtailed the gamma component by a factor of about 311, while the neutron component saw a reduction by a factor close to 58. Given the pronounced disparity in magnitude between these components, it's viable to look into the detector's count rate in the presence and absence of the gamma shielding. A decline from 522 to 48 was noted

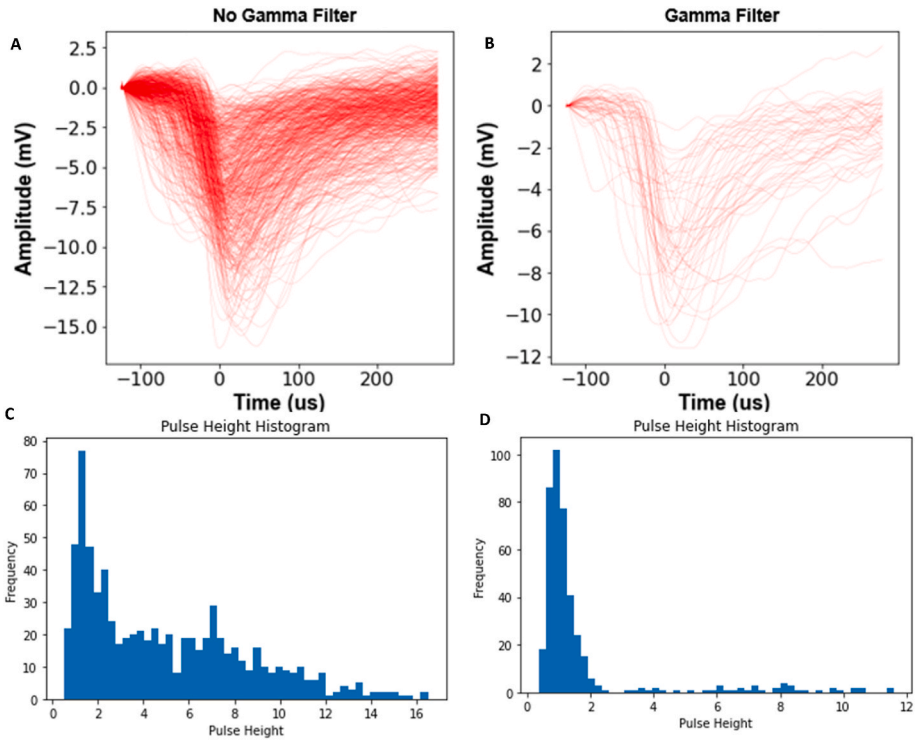

Fig. 6. (A–B) Pulses generated from the detector after being passed through the LOWESS filter for the experiment without (A) and with (B) the gamma shielding in the beam. (C–D) Histograms of the pulse heights of the respective experiments without (C) and with (D) the gamma shielding in the beam.

in the count rate of pulses that surpassed 2 mV, translating to a reduction factor of 10.8. The decline in signal aligns more closely with the neutron reduction (i.e., 58) than that with gamma-rays (i.e., 311). Thus, we infer that the pulses observed in Fig. 6B predominantly originate from fast neutrons over gamma rays.

Pulses gathered underwent a smoothing filter, and the resultant pulse height was plotted in a histogram, as depicted in Fig. 6C and D. Even though the total number of pulses might seem insufficient for a definitive spectrum, there's a tangible continuum when juxtaposed with simulation data. A mild drop in the highest recorded pulse height was observed when the gamma shutter was closed. This can be linked to a combined effect of reduced neutron flux and the potential interactions of high-energy gamma rays in the beam with the detector. Calibration was infeasible due to the crystal's inconsistent stability over time. Additionally, the device's initial packaging prohibited the acquisition of an alpha spectrum using an Am-241 source.

4. Conclusion

In this study, we successfully grew a single crystal $MHyPbCl_3$ of ample size to test as a perovskite-based direct conversion fast neutron detector. The material's characterization revealed satisfactory $\mu\tau$ and resistance, vital for charge capture from recoiled protons following neutron interactions with hydrogen in $MHyPbCl_3$. When exposed to a fast neutron beam from a research reactor and applying a combination of gamma-ray shielding and thermal neutron removing configurations, the $MHyPbCl_3$ detector displayed a discernible response to fast neutrons, though it also reacted to gamma-rays. Notably, the predominant pulse responses occurred when the gamma shutter blocked the beam, suggesting a primary reaction to fast neutrons. Complementarily, GEANT4 simulations mirrored these experimental findings, further affirming the viability of a perovskite-based direct conversion neutron detector. Overall, our findings underscore $MHyPbCl_3$'s promising potential as a fast neutron detector based on direct charge collection, anticipating further enhancements in material dimensions and quality.

Declaration of competing interest

The authors declare that they have no known competing financial interests or personal relationships that could have appeared to influence the work reported in this paper. This research has been performed using funding received from the U.S. Department of Defense, Defense Threat Reduction Agency under Grant HDTRA-11910024.

Acknowledgment

We would like to acknowledge the support of OSU Nuclear Reactor Laboratory and the assistance of the reactor staff members for the irradiation services provided. We would also like to thank Dr. John McClory at Air Force Institute of Technology for his valuable discussions. This research has been performed using funding received from the U.S. Department of Defense, Defense Threat Reduction Agency under Grant HDTRA-11910024.

References

[1] R.T. Kouzes, J.H. Ely, L.E. Erikson, W.J. Kernan, D.L. Stephens, E.R. Siciliano, D. R. Weier, Neutron detection alternatives to 3He for national security applications, Nucl. Instrum. Methods Phys. Res. Sect. A Accel. Spectrom. Detect. Assoc. Equip. 623 (3) (2009) 1035–1045.
[2] D. Vartsky, M.B. Goldberg, D. Bar, D. Friedman, Fast-neutron radiography scanner for the detection of contraband in air cargo containers, Nucl. Instrum. Methods Phys. Res. Sect. A Accel. Spectrom. Detect. Assoc. Equip. 577 (3) (2007) 698–707.
[3] O.K. Harling, K.J. Riley, T.H. Newton, P.J. Binns, I. Auterinen, The fission converter based epithermal neutron irradiation facility at the Massachusetts Institute of Technology Reactor. Nuclear Science, IEEE Transactions on 53 (1) (2006) 261–268.
[4] L. Zaidi, M. Belgaid, S. Taskaev, R. Khelifi, Boron neutron capture therapy (BNCT): a review of principle, method, and clinical prospects, Radiat. Phys. Chem. 152 (2018) 34–41.
[5] J.O. Goldsten, T.H. Prettyman, Neutron detection methods for oil well logging, Rev. Sci. Instrum. 79 (1) (2008) 014501.
[6] F.U. Dowla, A. Ionita, Neutron well logging: state of the art in nuclear physics methods, Nucl. Instrum. Methods Phys. Res. Sect. A Accel. Spectrom. Detect. Assoc. Equip. 591 (1) (2008) 155–159.

[7] D.S. McGregor, J.K. Shultis, C.J. Solomon, Fast-neutron, coded-aperture imager, Nucl. Instrum. Methods Phys. Res. Sect. A Accel. Spectrom. Detect. Assoc. Equip. 500 (1–3) (2003) 272–294.
[8] J. Pérez, T. Cáceres, H. Barros, Neutron detection using a water Cherenkov detector, Nucl. Instrum. Methods Phys. Res. Sect. A Accel. Spectrom. Detect. Assoc. Equip. 708 (2013) 14–17.
[9] D. Vartsky, D. Bar, A. Eilam, A. Goldschmidt, G. Feldman, M. Gai, I. Orion, Fast-neutron detectors for homeland security applications, Nucl. Instrum. Methods Phys. Res. Sect. A Accel. Spectrom. Detect. Assoc. Equip. 531 (3) (2004) 157–163.
[10] K.M. Surovec, Master's thesis. Miniaturized Neutron Radiation Detector Using Boron-Nitride and Multi-Walled Carbon Nanotubes, Naval Postgraduate School, Monterey, California, 2023.
[11] S.A. Pozzi, S.D. Clarke, D. Chichester, Chapter 1 - introduction to radiation detection systems, in: S.A. Pozzi, S.D. Clarke, D. Chichester (Eds.), Nuclear Nonproliferation, Elsevier, 2016, pp. 1–37, https://doi.org/10.1016/B978-0-12-803843-2.00001-7.
[12] R. Lopez, W.M. Steinberger, N. Giha, P. Marleau, S.D. Clarke, S.A. Pozzi, Neutron and gamma imaging using an organic glass scintillator handheld dual particle imager, Nucl. Instrum. Methods Phys. Res. Sect. A Accel. Spectrom. Detect. Assoc. Equip. 1042 (2022) 167407, https://doi.org/10.1016/j.nima.2022.167407. ISSN 0168-9002.
[13] F.D. Brooks, F.D. Smit, Scintillation efficiencies of stilbene crystals for fast neutrons, Nucl. Instrum. Methods Phys. Res. Sect. A Accel. Spectrom. Detect. Assoc. Equip. 652 (1) (2011) 466–468.
[14] N.P. Zaitseva, A.M. Glenn, A.N. Mabe, M.L. Carman, C. Hurlbut, J.W. Inman, S. A. Payne, Plastic scintillators with efficient neutron/gamma pulse shape discrimination, Nucl. Instrum. Methods Phys. Res. Sect. A Accel. Spectrom. Detect. Assoc. Equip. 668 (2012) 88–93.
[15] J. Glodo, R. Hawrami, J. Tower, K.S. Shah, P. Wong, Cs2LiYCl6: Ce scintillators for thermal and fast neutron detection, IEEE Trans. Nucl. Sci. 54 (3) (2007) 718–722.
[16] P. Dorenbos, Fundamental understanding of scintillation yield in inorganic scintillators, IEEE Trans. Nucl. Sci. 60 (3) (2013) 1753–1765.
[17] R.T. Kouzes, J.H. Ely, L.E. Erikson, W.J. Kernan, D.L. Stephens, E.R. Siciliano, D. R. Weier, Neutron detection alternatives to 3He for national security applications, Nucl. Instrum. Methods Phys. Res. Sect. A Accel. Spectrom. Detect. Assoc. Equip. 623 (3) (2009) 1035–1045.
[18] M.F. Pérez, M.Z. Ali, Novel boron lined neutron detectors: applications and performance, Nucl. Instrum. Methods Phys. Res. Sect. A Accel. Spectrom. Detect. Assoc. Equip. 866 (2017) 171–181.
[19] D.S. McGregor, J.K. Shultis, C.J. Solomon, Lithium indium diselenide neutron detector performance, Nucl. Instrum. Methods Phys. Res. Sect. A Accel. Spectrom. Detect. Assoc. Equip. 500 (1–3) (2003) 272–294.
[20] W.B. Lewis, A uranium-lined ionization chamber for measuring slow neutron flux, Can. J. Res. 26 (2) (1948) 148–159.
[21] G.F. Knoll, Radiation Detection and Measurement, fourth ed., John Wiley & Sons, 2010.
[22] V.A. Li, F. Sutanto, T.M. Classen, S.A. Dazeley, I. Jovanovic, T.C. Wu, Evaluation of a positron-emission-tomography-based SiPM readout for compact segmented neutron imagers, Nucl. Instrum. Methods Phys. Res. 1046 (2023) 167624, https://doi.org/10.1016/j.nima.2022.167624.
[23] V.A. Li, T.M. Classen, S.A. Dazeley, M.J. Duvall, I. Jovanovic, A.N. Mabe, E.T. E. Reedy, F. Sutanto, A prototype for SANDD: a highly-segmented pulse-shape-sensitive plastic scintillator detector incorporating silicon photomultiplier arrays, Nucl. Instrum. Methods Phys. Res. 942 (2019) 162334, https://doi.org/10.1016/j.nima.2019.162334.
[24] A. Buffler, A. Comrie, T. Hutton, A compact direction-sensitive fast neutron spectrometer, Nucl. Instrum. Methods Phys. Res. 1052 (2023) 168256, https://doi.org/10.1016/j.nima.2023.168256.
[25] M. Grodzicka- Kobylka, T. Szczesniak, L. Swiderski, K. Brylew, M. Moszyński, J. J. Valiente-Dobón, P. Schotanus, K. Grodzicki, P. Mazerewicz, J. Szymanowski, Z. Mianowska, Comparison of detectors with pulse shape discrimination capability for simultaneous detection of gamma-rays, slow and fast neutrons, Nucl. Instrum. Methods Phys. Res. 1019 (2021) 165858, https://doi.org/10.1016/j.nima.2021.165858.
[26] S.A. Richards, W. Helbsy, G.J. Sykora, R.M. Wheater, M.D. Wilson, Real-time pulse shape discrimination for neutron scattering science using EJ-270, J. Inst. Met. 17 (2022) P08011, https://doi.org/10.1088/1748-0221/17/08/P08011.
[27] S. Richards, G.J. Sykora, M.P. Taggart, High count rate pulse shape discrimination algorithms for neutron scattering facilities, Nucl. Instrum. Methods Phys. Res. 989 (2021) 164946, https://doi.org/10.1016/j.nima.2020.164946.
[28] F. Shen, Y. Pan, Q. Fu, S. Lin, T. Huang, W. Wang, PSD performance of EJ-276 and EJ-301 scintillator readout with SiPM array, Nucl. Instrum. Methods Phys. Res. 1039 (2022) 167148, https://doi.org/10.1016/j.nima.2022.167148.
[29] Gyanendra Bhattarai, Anthony N. Caruso, Michelle M. Paquette, Single-carrier charge collection in thin direct-conversion semiconductor neutron detector: a numerical simulation, J. Appl. Phys. 129 (19) (2021) 194502, https://doi.org/10.1063/5.0039034, 21 May.
[30] L. Carman, et al., Solution-grown rubrene crystals as radiation detecting devices, IEEE Trans. Nucl. Sci. 64 (2) (Feb. 2017) 781–788, https://doi.org/10.1109/TNS.2017.2652139.
[31] Y. Liu, H. Ye, Y. Zhang, K. Zhao, Z. Yang, Y. Yuan, et al., Surface-tension-controlled crystallization for high-quality 2D perovskite single crystals for ultrahigh photodetection, Matter 1 (2019) 465–480, https://doi.org/10.1016/j.matt.2019.04.002.
[32] Inrad Optics. (Year). Scintinel™ Stilbene for Fast Neutron Detection. Retrieved from https://inradoptics.com/pdfs/Inrad_AN_Stilbene.pdf.
[33] M. Mączka, A. Gagor, J.K. Zaręba, D. Stefanska, M. Drozd, S. Balciunas, et al., Three-dimensional perovskite methylhydrazinium lead chloride with two polar phases and unusual second-harmonic generation bistability above room temperature, Chem. Mater. 32 (2020) 4072–4082, https://doi.org/10.1021/acs.chemmater.0c00973.
[34] Jinxiao Zheng, Yan Zeng, Jingjing Wang, Chenghua Sun, Bin Tang, Yang Wu, Yuan Zhang, Yuanping Yi, Nü Wang, Yong Zhao, Shuyun Zhou, Hydrogen-rich 2D halide perovskite scintillators for fast neutron radiography, Nucl. Instrum. Methods Phys. Res., Sect. A 143 (50) (2021) 21302–21311, https://doi.org/10.1021/jacs.1c08923.
[35] S. Agostinelli, et al., GEANT4—a simulation toolkit, Nucl. Instrum. Methods Phys. Res. 506 (3) (2003) 250–303, https://doi.org/10.1016/S0168-9002(03)01368-8. Section A.
[36] S. Incerti, et al., The GEANT4-DNA project, Int. J. Modeling, Simulation, and Scientific Computing 1 (2) (2010) 157–178, https://doi.org/10.1142/S1793962310000122.
[37] B.W. Blackburn, J.T. Johnson, S.M. Watson, D.L. Chichester, J.L. Jones, F. H. Ruddy, J.G. Seidel, R.W. Flammang, Fast Digitization and Discrimination of Prompt Neutron and Photon Signals Using a Novel Silicon Carbide Detector, 2007.